Supplement of Atmos. Chem. Phys., 17, 5703–5719, 2017
https://doi.org/10.5194/acp-17-5703-2017-supplement

Atmospheric Chemistry and Physics
Open Access

Supplement of

Fine particle pH and gas–particle phase partitioning of inorganic species in Pasadena, California, during the 2010 CalNex campaign

Hongyu Guo et al.

Correspondence to: Rodney J. Weber (rweber@eas.gatech.edu) and Athanasios Nenes (athanasios.nenes@gatech.edu)

1. Comparisons of inorganic species measurements between AMS (PM_1) and PILS-IC ($PM_{2.5}$)

Consistency ($R^2 \geq 0.8$) between AMS and PILS-IC was observed. AMS measured nominally PM_1, whereas PILS-IC measured $PM_{2.5}$. These results are similar with other inter-comparisons reported elsewhere (Hayes et al., 2013). A larger difference in slope for nitrate than sulfate is thought to be due to higher nitrate concentrations in the 1 to 2.5 µm size range. $PM_1/PM_{2.5}$ mass ratios, reported in the main text, differ from slopes shown below due to differences in contributions of lower concentrations to these parameters (ratio vs. slope).

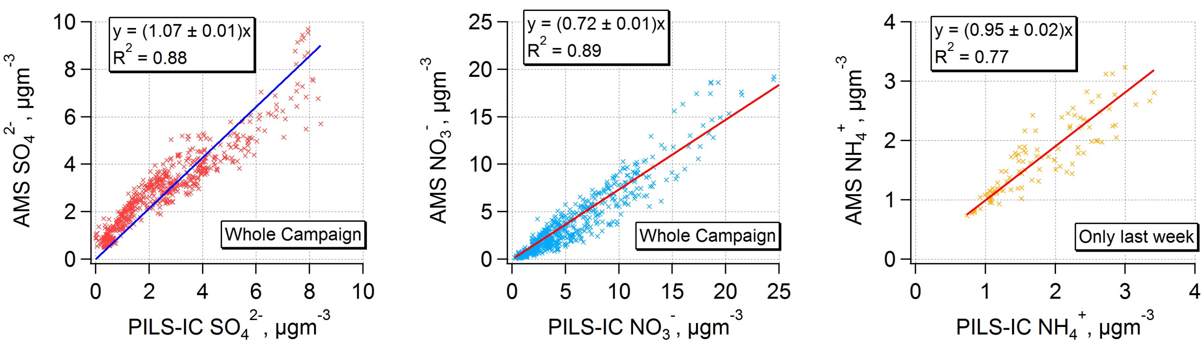

Fig. S1. Comparisons of PM_1 AMS sulfate, nitrate, ammonium to $PM_{2.5}$ PILS-IC (complete CalNex study except ammonium only for last week). Orthogonal distance regression (ODR) fits with fixed zero intercepts were applied. Fit slope uncertainty is one standard deviation.

2. The dependencies of nitrate, ammonium, and chloride on pH, W_i, and T (S curve equation derivations)

2.1 HNO_3-NO_3^- partitioning

The S curve of ε(NO_3^-) has been discussed explicitly and compared to observations from WINTER aircraft campaign in Guo et al. (2016). Here we show the detailed derivation of equation (3) in that paper. Equilibrium between gaseous HNO_3 and particle-phase NO_3^- involves two processes, first dissolution of HNO_3 into aqueous phase (assuming particles are liquids) and second dissociation of dissolved HNO_3 into H^+ and NO_3^-. The two processes are reversible and often reach thermodynamic equilibriums at ambient conditions (RH, T) for fine particles.

$$1^{st} \quad HNO_{3(g)} \leftrightarrow HNO_3, \quad H_{HNO_3}$$

$$2^{nd} \quad HNO_3 \leftrightarrow NO_3^- + H^+, \quad K_{n1}$$

for which reaction equilibriums are expressed as follows,

$$H_{HNO_3} = \gamma_{HNO_3}[HNO_3]/p_{HNO_3} \tag{1}$$

$$K_{n1} = \frac{\gamma_{NO_3^-}[NO_3^-]\gamma_{H^+}[H^+]}{\gamma_{HNO_3}[HNO_3]} \tag{2}$$

where H_{HNO_3} is HNO_3 Henry's law constant, K_{n1} is HNO_3 acid dissociation constant, γ represents activity coefficient, p_{HNO_3} is partial pressure of HNO_3 in atmosphere, and [x] represents aqueous concentrations (mole L^{-1}). From equations (1) and (2) we get the total dissolved HNO_3 or total particle-phase nitrate (${NO_3}^{T}$) as

$$[{NO_3}^{T}] = [HNO_3] + [NO_3^-] = H_{HNO_3}p_{HNO_3}\left(\frac{1}{\gamma_{HNO_3}} + \frac{K_{n1}}{\gamma_{NO_3^-}\gamma_{H^+}[H^+]}\right) \tag{3}$$

Ideal gas law gives

$$c(HNO_3) = \frac{p_{HNO_3}}{RT} \tag{4}$$

where c(x) represents concentration per volume of air (mole m^{-3}). Therefore, the particle-phase fraction of nitrate is

$$\varepsilon({NO_3}^{T}) = \frac{c(NO_3^T)}{c(HNO_3) + c(NO_3^T)} = \frac{[NO_3^T]W_i}{c(HNO_3) + [NO_3^T]W_i} \tag{5}$$

where W_i is the particle liquid water content associated with inorganic species (μg m^{-3}; mass per volume of air) (here the organics associated liquid water is not considered, but it can be included, or measured particle water can be used). Taking equations (3) and (4) into (5), we get $\varepsilon({NO_3}^{T})$ as

$$\varepsilon({NO_3}^{T}) = \frac{\left(\frac{\gamma_{NO_3^-}\gamma_{H^+}}{\gamma_{HNO_3}}[H^+] + K_{n1}\right) H_{HNO_3} W_i RT}{\gamma_{NO_3^-}\gamma_{H^+}[H^+] + \left(\frac{\gamma_{NO_3^-}\gamma_{H^+}}{\gamma_{HNO_3}}[H^+] + K_{n1}\right) H_{HNO_3} W_i RT} \tag{6}$$

At 298 K, K_{n1}=12 mole L^{-1} (Fountoukis and Nenes, 2007) often >> $\frac{\gamma_{NO_3^-}\gamma_{H^+}}{\gamma_{HNO_3}}[H^+]$, so we assume $\left(\frac{\gamma_{NO_3^-}\gamma_{H^+}}{\gamma_{HNO_3}}[H^+] + K_{n1}\right) \approx K_{n1}$. Thus, a simplified equation is

$$\varepsilon({NO_3}^{T}) \cong \frac{K_{n1} H_{HNO_3} W_i RT}{\gamma_{NO_3^-}\gamma_{H^+}[H^+] + K_{n1} H_{HNO_3} W_i RT} \tag{7}$$

$H_{HNO_3} K_{n1}$ is denoted as $H^*_{HNO_3}$ (mole^2 kg^{-2} atm^{-1}) hereafter, which is equilibrium constant of the combined dissolution and deprotonation processes as,

$$HNO_{3(g)} \leftrightarrow {NO_3}^- + H^+, \quad H^*_{HNO_3}$$

$H^*_{HNO_3}$ can be easily calculated by equation (40) in Clegg and Brimblecombe (1990) for T dependence and converted from unit atm^{-1} (mole fraction based) to mole^2 kg^{-2} atm^{-1} (molality based) by equation (5) also in that paper. To be consistent with SI units, we have the following equation ready for users' input:

$$\begin{aligned}\varepsilon({NO_3}^{T}) &\cong \frac{H^*_{HNO_3} W_i RT \times 0.987 \times 10^{-14}}{\gamma_{NO_3^-}\gamma_{H^+}[H^+] + H^*_{HNO_3} W_i RT \times 0.987 \times 10^{-14}} \\ &= \frac{H^*_{HNO_3} W_i RT \times 0.987 \times 10^{-14}}{\gamma_{NO_3^-}\gamma_{H^+} 10^{-pH} + H^*_{HNO_3} W_i RT \times 0.987 \times 10^{-14}}\end{aligned} \tag{8}$$

Note that 0.987 comes from the conversion from 1 atm to 1 bar and W_i unit is µg m^{-3}. Equation (8) describes the dependence of HNO_3-NO_3^- partitioning on pH, T, and W_i (determined by RH and aerosol composition). Based on ideal and non-ideal aqueous particles, several $\varepsilon({NO_3}^-)$ S curves at atmosphere relevant conditions are plotted together with $\varepsilon(Cl^-)$ and $\varepsilon({NH_4}^+)$ in Fig S3 and S4, respectively.

$\varepsilon({NO_3}^{T})$ is equivalent to $\varepsilon({NO_3}^-)$ in the main text, since NO_3^- is practically 100% of NO_3^T based on $K_{n1} \gg \frac{\gamma_{NO_3^-}\gamma_{H^+}}{\gamma_{HNO_3}}[H^+]$ (also under atmospheric condition). The fraction of NO_3^- over NO_3^T can be given as

$$\frac{[{NO_3}^-]}{[{NO_3}^{T}]} = \frac{K_{n1}}{K_{n1} + \frac{\gamma_{NO_3^-}\gamma_{H^+}}{\gamma_{HNO_3}}[H^+]} \tag{9}$$

2.2 HCl-Cl$^-$ partitioning

Following the same derivation procedure as HNO_3-NO_3^- partitioning, we have $\varepsilon(Cl^-)$ as

$$\varepsilon(Cl^-) \cong \frac{H^*_{HCl} W_i RT \times 0.987 \times 10^{-14}}{\gamma_{Cl^-}\gamma_{H^+}[H^+] + H^*_{HCl} W_i RT \times 0.987 \times 10^{-14}} = \frac{H^*_{HCl} W_i RT \times 0.987 \times 10^{-14}}{\gamma_{Cl^-}\gamma_{H^+}10^{-pH} + H^*_{HCl} W_i RT \times 0.987 \times 10^{-14}} \quad (10)$$

where H^*_{HCl} (mole^2 kg^{-2} atm^{-1}) is the equilibrium constant and is equal to the "conventional" Henry's law constant multiplied by the acid dissociation constant of hydrochloric acid. H^*_{HCl} can be calculated by equation (22) in Carslaw et al. (1995) to account for T's variation.

$$HCl_{(g)} \leftrightarrow Cl^- + H^+, \quad H^*_{HCl}$$

A comparison of $\varepsilon(Cl^-)$ S curve with a subset of CalNex data is shown in Fig. S2. The selected CalNex data are all in a small range of T 15.5 to 19.5 ºC (around campaign average T) and W_i 10 to 20 µg m^{-3}, while the S curve is calculated based on the average condition of these data as T = 17.5 ºC, W_i = 15 µg m^{-3}, $\gamma_{H^+-Cl^-}$ = 0.81 (The binary activity coefficient, $\gamma_{H^+-Cl^-} = \sqrt{\gamma_{H^+}\gamma_{Cl^-}}$). The distribution of the $\varepsilon(Cl^-)$ points close to S curve validates the $PM_{2.5}$ pH prediction and demonstrates the usage of S curve.

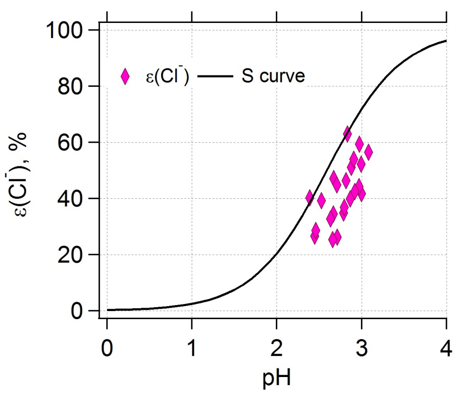

Fig. S2. The comparison of S curve and measured ε(Cl^-) with predicted particle pH by ISORROPIA-II. Cl^- is from $PM_{2.5}$ PILS-IC measurements.

2.3 NH_3-NH_4^+ partitioning

The derivation of NH_3-NH_4^+ partitioning is a bit different from the above two acidic gases. Equilibrium between gaseous NH_3 and NH_4^+ can be described simply as

$$NH_{3(g)} + H^+ \leftrightarrow NH_4{}^+, \quad H^*_{NH_3}$$

($H^*_{NH_3}$ is equivalent to the "conventional" Henry's law constant of NH_3 divided by the acid dissociation constant of NH_4^+) or described by the follow two reversible reactions assuming water activity as unity.

$$1^{st} \quad NH_{3(g)} \leftrightarrow NH_3, \qquad H_{NH_3}$$

$$2^{nd} \quad NH_3 + H^+ \leftrightarrow NH_4^+, \quad 1/K_a$$

for which reaction equilibriums are described as

$$H_{NH_3} = \gamma_{NH_3}[NH_3]/p_{NH_3} \tag{11}$$

$$1/K_a = \frac{\gamma_{NH_4^+}[NH_4^+]}{\gamma_{NH_3}[NH_3]\gamma_{H^+}[H^+]} \tag{12}$$

where H_{NH_3} is NH_3 Henry's law constant, K_a is NH_4^+ acid dissociation constant, γ represents activity coefficient, p_{NH_3} is partial pressure of NH_3 in atmosphere, and [x] represents aqueous concentrations (mole L^{-1}). Please note that the 2nd reaction is usually written in another form (Fountoukis and Nenes, 2007) as

$$2^{nd} \quad NH_3 + H_2O \leftrightarrow NH_4^+ + OH^-, \quad K_w/K_a$$

where K_w is water dissociation constant. Equations (10) and (11) give the total dissolved NH_3 or total particle-phase ammonium (NH_4^{T}) as

$$[NH_4^T] = [NH_3] + [NH_4^+] = H_{NH_3}p_{NH_3}\left(\frac{1}{\gamma_{NH_3}} + \frac{\gamma_{H^+}[H^+]}{\gamma_{NH_4^+}K_a}\right) \tag{13}$$

Combining with ideal gas law, that is

$$c(NH_3) = \frac{p_{NH_3}}{RT} \tag{14}$$

where c(x) represents concentration per volume of air (mole m^{-3}). We have the particle-phase fraction of ammonium as

$$\varepsilon(NH_4^{\mathrm{T}}) = \frac{c(NH_4^T)}{c(NH_3) + c(NH_4^T)} = \frac{[NH_4^T]W_i}{c(NH_3) + [NH_4^T]W_i} \tag{15}$$

With equations (12) and (13), the above equation is transformed into

$$\varepsilon(NH_4^{\mathrm{T}}) = \frac{\left(\frac{\gamma_{H^+}[H^+]}{\gamma_{NH_4^+}} + \frac{K_a}{\gamma_{NH_3}}\right)\frac{H_{NH_3}}{K_a}W_iRT}{1 + \left(\frac{\gamma_{H^+}[H^+]}{\gamma_{NH_4^+}} + \frac{K_a}{\gamma_{NH_3}}\right)\frac{H_{NH_3}}{K_a}W_iRT} \tag{16}$$

At 298 K, K_a = 5.69×10^{-10} mole L^{-1} (Clegg et al., 1998) results in $\frac{K_a}{\gamma_{NH_3}} \ll \frac{\gamma_{H^+}[H^+]}{\gamma_{NH_4^+}}$ as long as the solution is not too basic. Neglecting $\frac{K_a}{\gamma_{NH_3}}$ part and taking $\frac{H_{NH_3}}{K_a} = H^*_{NH_3}$, we have

$$\varepsilon(NH_4^{\mathrm{T}}) \cong \frac{\frac{\gamma_{H^+}[H^+]}{\gamma_{NH_4^+}}H^*_{NH_3}W_iRT}{1 + \frac{\gamma_{H^+}[H^+]}{\gamma_{NH_4^+}}H^*_{NH_3}W_iRT} \tag{17}$$

To be consistent with SI units, the equation (16) is then presented as:

$$\varepsilon(NH_4^{\mathrm{T}}) \cong \frac{\frac{\gamma_{H^+}[H^+]}{\gamma_{NH_4^+}} H^*_{NH_3} W_i RT \times 0.987 \times 10^{-14}}{1 + \frac{\gamma_{H^+}[H^+]}{\gamma_{NH_4^+}} H^*_{NH_3} W_i RT \times 0.987 \times 10^{-14}} = \frac{\frac{\gamma_{H^+} 10^{-pH}}{\gamma_{NH_4^+}} H^*_{NH_3} W_i RT \times 0.987 \times 10^{-14}}{1 + \frac{\gamma_{H^+} 10^{-pH}}{\gamma_{NH_4^+}} H^*_{NH_3} W_i RT \times 0.987 \times 10^{-14}} \quad (18)$$

where the 0.987 comes from the conversion from 1 atm to 1 bar and W_i unit is μg m^{-3}. $H^*_{NH_3}$(atm^{-1}) can be calculated from equation (12) in Clegg et al. (1998) following a typo correction to the equation. The corrected equation is:

$$\ln(H^*_{NH_3}) = 25.393 - 10373.6(1/T_r - 1/T) + 4.131(T_r/T - (1 + \ln(T_r/T))) \quad (19)$$

where T_r is the reference temperature of 298.15 K. Note that, the mole fraction based $H^*_{NH_3}$ has the same numerical value as its molality based form. After correction, a larger $H^*_{NH_3}$ is associated with a lower temperature, consistent with a general expectation that NH_3 condenses onto particles if temperature decreases. ε(NH_4^{T}) is equivalent to ε(NH_4^+) presented in the main text, since NH_4^+ is the dominant form of dissolved NH_3 based on $\frac{K_a}{\gamma_{NH_3}} \ll \frac{\gamma_{H^+}[H^+]}{\gamma_{NH_4^+}}$ and under atmospheric conditions.

Summary: with the equations of ε(NO_3^-), ε(Cl^-), and ε(NH_4^+), S-shaped curves of these three paired gas to particle partitioning can be easily calculated with pH, T, W_i, and activity coefficients. We simulate two set of results, Fig S3 assuming activity coefficients to be one (ideal solution) and Fig S4 with practical activity coefficients from CalNex.

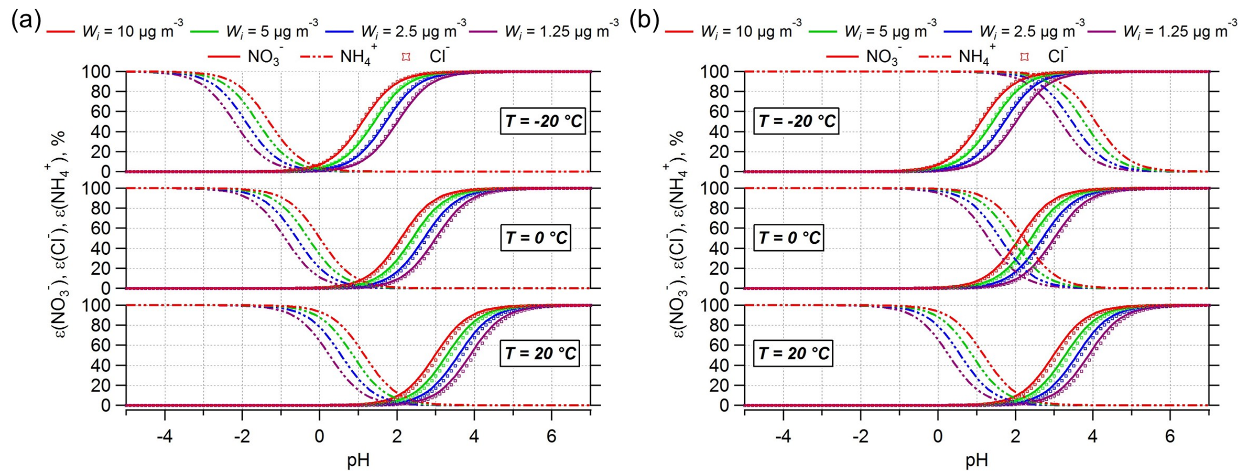

Fig. S3. Simulated ε(NO_3^-), ε(NH_4^+), ε(Cl^-) at -20 °C, 0 °C, 20 °C and various particle liquid water levels (1.25, 2.5, 5, 10 µg m^{-3}) assuming ideal solutions. Note that Fig. S3a shows ε(NH_4^+) calculated using the equation (12) in Clegg et al. (1998), and Fig. S3b shows ε(NH_4^+) using the corrected equation, given above as equation (19). The correct equation for $H_{NH_3}^*$ shifts ε(NH_4^+) to higher pH at lower T, as expected.

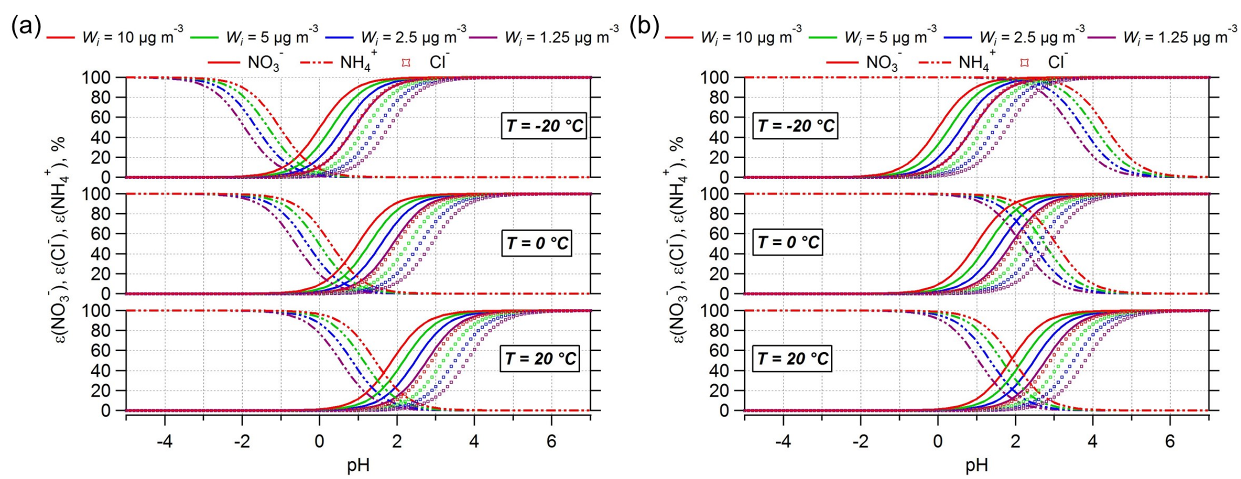

Fig. S4. Simulated ε(NO_3^-), ε(NH_4^+), ε(Cl^-) at -20 °C, 0 °C, 20 °C and various particle liquid water levels (1.25, 2.5, 5, 10 µg m^{-3}) with activity coefficients obtained from CalNex campaign. $\gamma_{H^+-NO_3^-}$ = 0.28, $\gamma_{H^+-Cl^-}$ = 0.81, and $\gamma_{H^+}/\gamma_{NH_4^+}$ = 1.90. Similar to Fig. S3, Fig. S4a shows ε(NH_4^+) calculated using the equation (12) in Clegg et al. (1998), and Fig. S4b shows ε(NH_4^+) using the corrected equation, given above as equation (19).

3. Investigation of the cause for bias in ε(NO_3^-): sample line heating?

As Fig. S5 shows, NO_3^- and ε(NO_3^-) are both over-predicted during the nighttime and under-predicted during the daytime. The deviations from measurements are anti-correlated with nitric acid. The deviation between predicted and measured HNO_3 also has a diurnal pattern, reverse to that of NO_3^-.

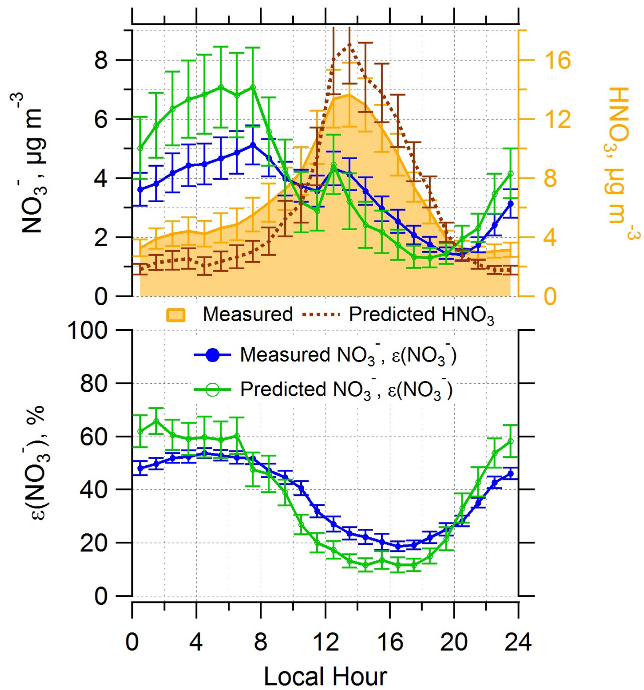

Fig. S5. Diurnal profiles of measured and predicted HNO_3, NO_3^-, and ε(NO_3^-). Data shown above are for the complete CalNex study and particle-phase data is AMS PM_1. Mean hourly averages are shown and standard errors are plotted as error bars.

Table S1. Summary of temperature differences in sample lines and ambient and sample line residence time for the AMS and CIMS. AMS indoor T was 25°C. CIMS inlet was heated to 75°C.

Instrument	Inlet residence time, sec	Time of the day	Temperature differences, °C
AMS	2.1	Day Night	~0 ~ +10
CIMS	0.32	Day Night	~ +50 ~ +60

For the AMS sample line located indoors, particle heating was most likely to occur at night (indoor T > ambient T), which may cause semi-volatile NO_3^- loss. There were no temperature differences during the day (Table S1). To examine the possible sample line heating/cooling effect, we first determined sample line RH (Equation 20) by conservation of water vapor under isobaric condition and following saturated water vapor pressure equation $e_s = 6.11\times10^{\left(\frac{7.5T}{237.5+T}\right)}$ (T unit as °C) (Alduchov and Eskridge, 1996). The inferred sample line RH is plotted with measured ambient RH in Fig. S6b. Sample line RH was lower (~50%) than ambient (~90%) at midnight and close to ambient (~60%) in the afternoon since temperatures were similar.

$$RH_2 = RH_1 10^{\left[\left(\frac{7.5T_1}{237.5+T_1}\right)-\left(\frac{7.5T_2}{237.5+T_2}\right)\right]} \quad (20)$$

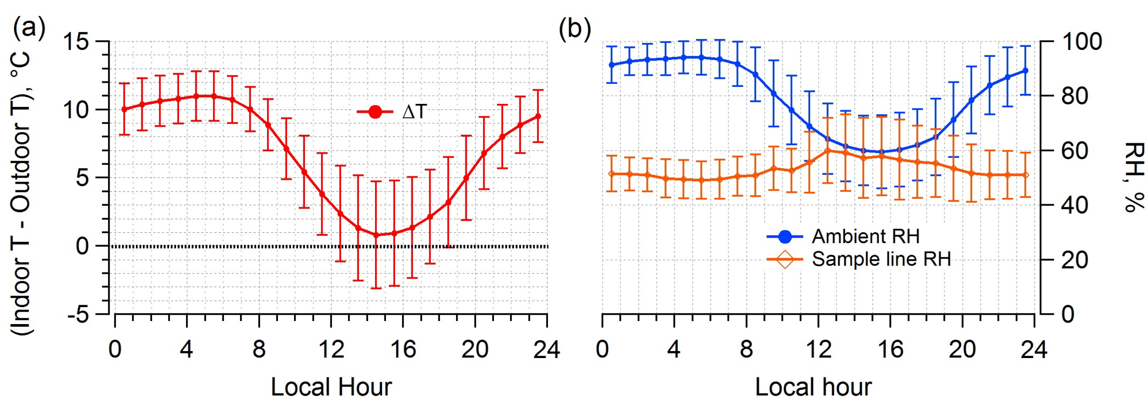

Fig. S6. Diurnal profiles of (a) temperature difference between AMS indoor and outdoor and (b) corresponding ambient and RH predicted in the sample line due to the T difference. Mean hourly averages and standard deviations are shown.

ISORROPIA-II was run with aerosol and gas-phase species at the AMS sample line T and RH and compared to predictions from ambient T and RH and measurements. Fig. S7 is discussed in the main text section 4.1.

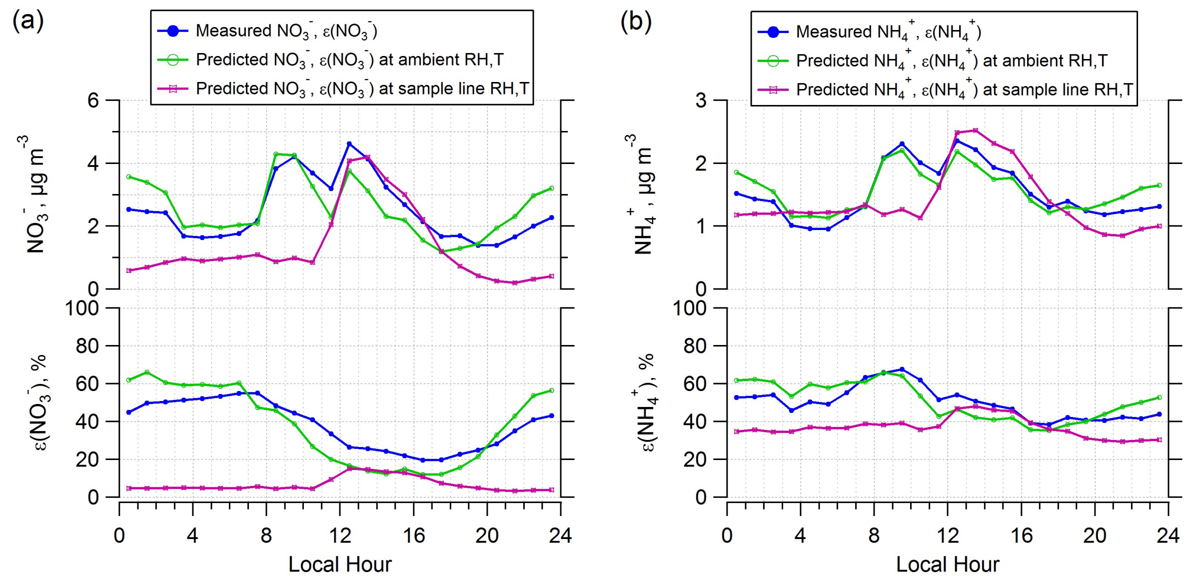

Fig. S7. Diurnal profiles of measured and predicted (a) NO_3^-, $\varepsilon(NO_3^-)$ and (b) NH_4^+, $\varepsilon(NH_4^+)$. Predictions are based on ambient or sample line RH and T for AMS inlet. Data shown above are for the complete CalNex study in the 20-95% RH range and particle-phase data is AMS PM_1. Mean hourly averages are shown. ISORROPIA run with ambient data show that the predicted partitioning between the particle and gas phase is in better agreement with observations than runs using sample line T and RH. Note that in both runs, only T and RH differ since total nitrate and ammonium input are the same.

CIMS inlet heating is similar for day (~50°C) and night (~60°C). Potential bias in the HNO_3 or HCl then mainly depends on the mass loadings of NO_3^- or Cl^-. Here we focus only on the possible bias due to over-measurement of HNO_3. ISORROPIA-II was run at ambient RH and T with a "corrected" HNO_3 at three assumed lower levels of HNO_3 to compensate for an assumed positive nitrate artifact of 10%, 20%, 30% (i.e., assuming 10, 20 or 30% of the nitrate measured by the AMS or PILS was evaporated in the CIMS inlet leading to an over-measurement of HNO_3. 10% to 30% particle NO_3^- was subtracted from the measured CIMS HNO_3). Only HNO_3 is modified, all other inputs are kept the same. Results are shown in Fig. S8. Evaporation of 30% of the measured nitrate is expected to be an extreme upper limit. For instance, 66% of PM_1 nitrate evaporated at a temperature of 75°C in a thermal denuder upstream of the AMS at the CalNex site, consistent with previous results at other urban sites in the LA area and elsewhere (Huffman et al., 2009). The residence time on the thermal denuder was ~ 12 sec, while that of the CIMS inlet was ~0.32 sec, so the extent of evaporation in the CIMS inlet assumed to be substantially lower than that in the thermal denuder.

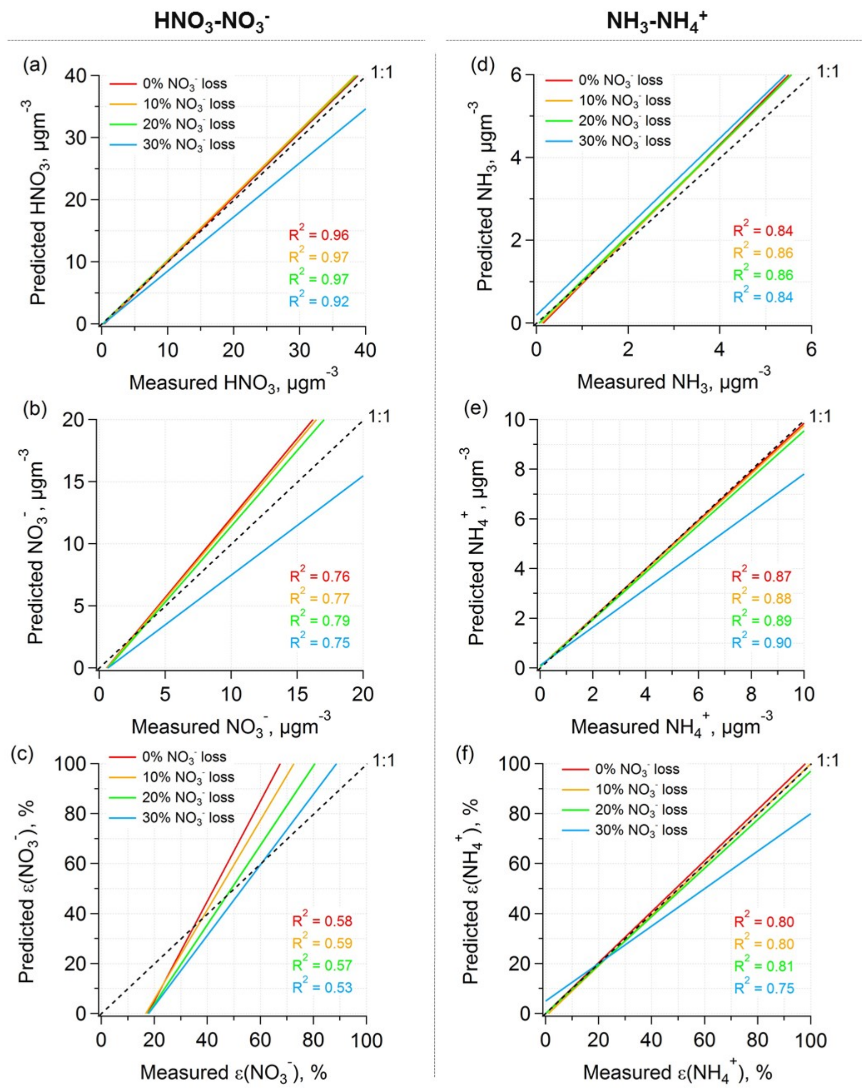

Fig. S8. Comparisons of predicted and measured HNO_3, NO_3^-, and $\varepsilon(NO_3^-)$ (a, b, c) and NH_3, NH_4^+, and $\varepsilon(NH_4^+)$ (d, e, f) for data from the complete CalNex study based on "corrected" HNO_3 data due to assumed PM_1 nitrate evaporation in the heated CIMS inlet. The other inputs are kept the same. Only the orthogonal regression fits are shown. "0% NO_3^- loss" condition is the same as Figure 2 in the main text.

References

Alduchov, O. A., and Eskridge, R. E.: Improved magnus form approximation of saturation vapor pressure, J Appl Meteorol, 35, 601-609, doi: 10.1175/1520-0450(1996)035<0601:Imfaos>2.0.Co;2, 1996.

Carslaw, K. S., Clegg, S. L., and Brimblecombe, P.: A Thermodynamic Model of the System HCl-HNO_3-H_2SO_4-H_2O, Including Solubilities of Hbr, from <200 to 328 K, Journal of Physical Chemistry, 99, 11557-11574, doi: 10.1021/j100029a039, 1995.

Clegg, S. L., and Brimblecombe, P.: Equilibrium Partial Pressures and Mean Activity and Osmotic Coefficients of 0-100-Percent Nitric-Acid as a Function of Temperature, Journal of Physical Chemistry, 94, 5369-5380, doi: 10.1021/j100376a038, 1990.

Clegg, S. L., Brimblecombe, P., and Wexler, A. S.: Thermodynamic model of the system H^+-NH_4^+-SO_4^{2-}-NO_3^--H_2O at tropospheric temperatures, J Phys Chem A, 102, 2137-2154, doi: 10.1021/Jp973042r, 1998.

Fountoukis, C., and Nenes, A.: ISORROPIA II: a computationally efficient thermodynamic equilibrium model for K^+-Ca^{2+}-Mg^{2+}-NH_4^+-Na^+-SO_4^{2-}-NO_3^--Cl^--H_2O aerosols, Atmospheric Chemistry and Physics, 7, 4639-4659, doi: 10.5194/acp-7-4639-2007, 2007.

Guo, H., Sullivan, A. P., Campuzano-Jost, P., Schroder, J. C., Lopez-Hilfiker, F. D., Dibb, J. E., Jimenez, J. L., Thornton, J. A., Brown, S. S., Nenes, A., and Weber, R. J.: Fine particle pH and the partitioning of nitric acid during winter in the northeastern United States, Journal of Geophysical Research: Atmospheres, 121, 10,355-310,376, doi: 10.1002/2016jd025311, 2016.

Hayes, P. L., Ortega, A. M., Cubison, M. J., Froyd, K. D., Zhao, Y., Cliff, S. S., Hu, W. W., Toohey, D. W., Flynn, J. H., Lefer, B. L., Grossberg, N., Alvarez, S., Rappenglück, B., Taylor, J. W., Allan, J. D., Holloway, J. S., Gilman, J. B., Kuster, W. C., de Gouw, J. A., Massoli, P., Zhang, X., Liu, J., Weber, R. J., Corrigan, A. L., Russell, L. M., Isaacman, G., Worton, D. R., Kreisberg, N. M., Goldstein, A. H., Thalman, R., Waxman, E. M., Volkamer, R., Lin, Y. H., Surratt, J. D., Kleindienst, T. E., Offenberg, J. H., Dusanter, S., Griffith, S., Stevens, P. S., Brioude, J., Angevine, W. M., and Jimenez, J. L.: Organic aerosol composition and sources in Pasadena, California, during the 2010 CalNex campaign, Journal of Geophysical Research: Atmospheres, 118, 9233-9257, doi: 10.1002/jgrd.50530, 2013.

Huffman, J. A., Docherty, K. S., Aiken, A. C., Cubison, M. J., Ulbrich, I. M., DeCarlo, P. F., Sueper, D., Jayne, J. T., Worsnop, D. R., Ziemann, P. J., and Jimenez, J. L.: Chemically-resolved aerosol volatility measurements from two megacity field studies, Atmospheric Chemistry and Physics, 9, 7161-7182, doi: 10.5194/acp-9-7161-2009, 2009.